Advanced Materials Interfaces

ADVANCED MATERIALS INTERFACES Open Access

www.advmatinterfaces.de

RESEARCH ARTICLE OPEN ACCESS

Ultraflat Honeycomb Stanene Nanoribbons on Au(111)

Julian Andreas Hochhaus[1,2] | Stefanie Hilgers[1,2] | Alexander Kononov[1] | Philipp Weinert[1,2] | Ulf Berges[1,2] | Heinz Hövel[1] | Carsten Westphal[1,2]

[1]Department of Physics, TU Dortmund University, Dortmund, Germany | [2]DELTA, Center for Synchrotron Radiation, TU Dortmund University, Dortmund, Germany

Correspondence: Julian Andreas Hochhaus (julian.hochhaus@tu-dortmund.de)

Received: 18 September 2025 | **Revised:** 11 November 2025 | **Accepted:** 13 November 2025

Keywords: epitaxial growth | interface | nanoribbons | stanene | structural evolution

ABSTRACT

Sn on Au(111) undergoes a structural and chemical evolution depending on the submonolayer coverage. After deposition of $\approx 2/3$ ML Sn, the coverage was controlled by temperature-driven desorption. Annealing to 450 K produced the striped phase, which consists of alternating honeycomb and square-like Sn stripes, with periodicities ranging from Rec($13 \times 2\sqrt{3}$) to Rec($19 \times 2\sqrt{3}$), most commonly Rec($16 \times 2\sqrt{3}$). Honeycomb regions are atomically flat, with a Sn–Sn bond length of $\approx$2.88 Å. Low-energy electron diffraction (LEED), atomically resolved scanning tunneling microscopy (STM), and X-ray photoelectron spectroscopy (XPS) reveal structural and chemical transitions as a function of Sn coverage. Without further annealing, deposition yields a square-like X-phase atop an Au_2Sn interface alloy. Annealing induces dealloying and the formation of the striped phase, while further desorption produces a $\sqrt{7}$ stretched honeycomb phase. Annealing above 480 K, and at $\approx$ 0.35 ML coverage, the Au_2Sn alloy reforms.

For the striped phase, a model is proposed where square-like stripes grow on Au_2Sn regions and honeycomb stripes on Au(111). The alternating regions correspond to zigzag stanene nanoribbons of $\approx$ 1.5 nm to 3.2 nm width. The structural transitions of the Sn/Au(111) system highlight its structural versatility, driven by alloying–dealloying processes at the interface.

1 | Introduction

Two-dimensional counterparts of carbon-group elements have gained increasing attention in recent years. Among them, stanene, a single layer of tin atoms in a honeycomb lattice, has attracted particular interest due to its predicted topological and electronic properties. Theoretical studies suggest that stanene may host quantum spin Hall insulating phases, exhibit a band gap up to 300 meV, and support topological superconductivity [1–3].

Beyond the honeycomb lattice, other 2D tin arrangements have been studied by theory, such as pentamer and tetramer structures with rectangular unit cells [4] and bilayer square lattices [5]. Experimental realizations of silicene [6] and germanene nanoribbons [7] revealed strong substrate dependence, with topological phases sensitive to ribbon width and spin–orbit coupling strength. These findings motivated theoretical studies on stanene nanoribbons, a dependence of the band structure on the nanoribbon width and passivation, edge magnetic anisotropy arising from the strong spin–orbit coupling, and strain-driven spin-filtering properties have been observed [8–11]. However, experimental realization of stanene nanoribbons has not been reported yet.

The first experimental realization of stanene was reported on Bi_2Te_3 [12]. Since then, different substrates have been explored, including Sb(111), InSb(111), Pd_2Sn(111), and Cu(111), resulting in stanene ranging from ultraflat to buckled structure [13–16]. Theory proposes planar stanene growth on Au(111) due to its close lattice match and the predicted substrate bonding via

Sn–p_z orbitals, which stabilizes sp^2 interlayer bonding and planar growth [17].

Experimental studies of Sn/Au(111) identified a large variety of structural phases, including honeycomb-like stanene [18, 19] and surface alloys [20, 21]. A stretched honeycomb dimer phase has been reported with linearly dispersing bands, alternating spin polarization, and high Fermi velocities of $v_F = 1 \times 10^6\ ms^{-1}$ [22]. In our recent work, we identified a square-like Sn layer atop an Au_2Sn alloy layer, showing that Sn/Au(111) can adopt structures beyond the substrates' hexagonal symmetry [23].

In this work, we report on the discovery of a striped Sn phase formed on Au(111) through temperature-driven desorption. We show that post-deposition annealing allows precise control of the Sn coverage, which controls the structural arrangement at the surface and interface. After deposition of $\approx 2/3$ ML Sn, annealing to 450 K produces a previously unreported striped phase. Scanning tunneling microscopy (STM) and low-energy electron diffraction (LEED) reveal alternating honeycomb and square-like Sn stripes, with periodicities ranging from Rec($13 \times 2\sqrt{3}$) to Rec($19 \times 2\sqrt{3}$), most commonly Rec($16 \times 2\sqrt{3}$).

Using XPS, we tracked the chemical and structural evolution of Sn phases on Au(111) as a function of Sn coverage and post-deposition annealing temperature. Initially, the square-like X-phase forms atop a complete Au_2Sn surface alloy. Subsequent annealing drives dealloying and partial desorption of Sn, leading to the formation of the striped phase, with alternating square-like and honeycomb Sn stripes. Further desorption forms the $\sqrt{7}$-phase, a stretched honeycomb Sn-dimer arrangement on clean Au(111). At annealing above 480 K, realloying occurs, resulting in the reformation of a Au_2Sn surface alloy.

For the striped phase, we propose a model in which square-like stripes form on Au_2Sn-alloy regions, while the honeycomb stripes grow directly on Au(111). The honeycomb regions, separated by square-like stripes, correspond to zigzag stanene nanoribbons with widths between ≈ 1.5 nm and ≈ 3.2 nm. Our results demonstrate that alloying and dealloying at the Sn/Au(111) interface drives the formation of the different 2D Sn phases, including honeycomb stanene, square-like arrangements, ordered Sn-dimer layers, and nanoribbon-like structures.

2 | Results

Before studying the formation of Sn superstructures on Au(111), we verified the cleanliness of the Au(111) surface using LEED, STM, and XPS.

Preparation details and full characterization results are provided in the Supporting Information (see Figure S1). This data confirms the clean herringbone reconstruction and shows the Au 4f core level spectrum is composed of two components, which are identified as bulk and surface contributions (Table S1). As will be discussed later in the XPS analysis, this surface component is highly sensitive to interactions with the deposited Sn and is replaced by the Au-Sn alloy component as the Au_2Sn-alloy forms at a Sn coverage of ≈ 0.35 ML, which we analyzed in detail in a recent paper [24].

Figure 1 shows the structural evolution of the Sn/Au(111) system after deposition of ≈0.66 ML of Sn and annealing for 60 min at the temperatures indicated in the Figure for each phase.

When ≈0.66 ML of Sn is deposited at room temperature with minimal or no post-deposition annealing, the so-called X-phase forms. This complex, spot-rich reconstruction was first reported by Maniraj et al. [22], who described it using the reconstruction matrix $\left(\begin{smallmatrix} 3.58 & 0 \\ 1.96 & 3.92 \end{smallmatrix}\right)$. Following their terminology, we also refer to this structure as the X-phase. Pang et al. [18] identified the X-phase as a stretched/compressed $2 \times \sqrt{3}$ reconstruction. In our recent study, we observed for the X-phase a local Rec(1.925×1.925) square-like Sn arrangement with small lattice variations atop an Au_2Sn alloy layer, which results in a Rec(7.7×3.85) unit cell [23].

Reducing the Sn coverage to ≈0.55 ML by annealing the X-phase to ≈ 450 K, a new structural phase emerges, to which we refer as the striped phase. It is marked by stripe-like features in the LEED pattern, as shown in Figure 1. The transition into this phase is irreversible and driven by thermal desorption of Sn. While Maniraj et al. reported a mixed phase under similar preparation conditions [22], our data suggest that this reported mixed phase corresponds to a coexistence of the striped phase and the X-phase.

Further Sn desorption by annealing to ≈ 455 K results in the $\sqrt{7}$-phase, described by the matrix $\left(\begin{smallmatrix} 2 & 1 \\ 1 & 3 \end{smallmatrix}\right)$, which corresponds to a stretched $\sqrt{7} \times \sqrt{3}$ hexagonal structure. Maniraj et al. described this phase as Sn dimers in a stretched honeycomb arrangement. They measured a linearly dispersing band below the Fermi level, a Fermi velocity of $v_F = 1 \times 10^6\ ms^{-1}$, and alternating spin polarization [22]. Our structural analysis, presented in the Supporting Information (Section S2), is consistent with their proposed structural model.

When the sample is annealed above 480 K, at a coverage of ≈0.35 ML, the characteristic $(\sqrt{3} \times \sqrt{3})R30°$ LEED pattern of the Au_2Sn alloy appears [20, 25]. If the annealing temperature is further increased, the long-range order forms and the Rec($26 \times \sqrt{3}$) herringbone-like superstructure of the Au_2Sn alloy is observed [21, 24], which remains stable up to ≈ 700 K. Above this temperature, degradation of the reconstruction is observed in LEED. Annealing to ≈ 900 K results in the desorption of nearly all Sn atoms, with XPS indicating a residual coverage of ≤0.05 ML.

Although all superstructures discussed were prepared by depositing approximately 0.66 ML of Sn followed by annealing, we observed that the Au_2Sn alloy at the surface serves as a universal starting point for preparing these structures. Similar superstructures can also be obtained through alternative approaches. For instance, depositing around 0.3 ML of Sn onto the preformed Au_2Sn alloy, either created by room-temperature deposition of 0.35 ML Sn or by annealing structural phases with higher Sn coverages above 480 K, yields to the formation of the X-phase as well.

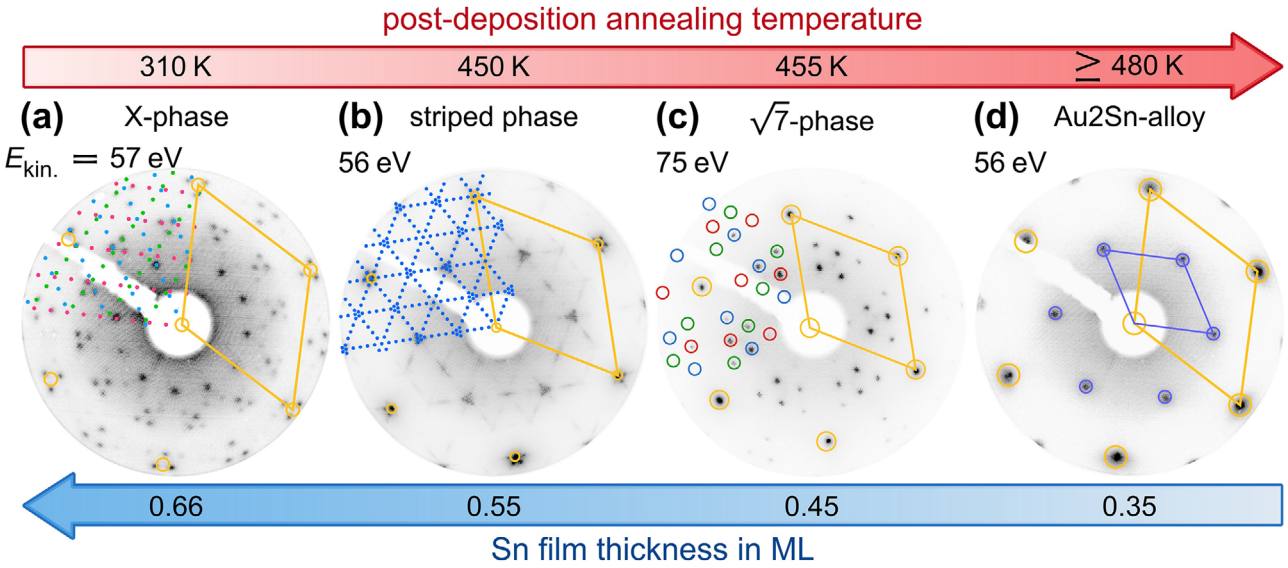

FIGURE 1 | LEED pattern showing the structural evolution of 0.66 ML Sn deposited on Au(111) at room temperature, followed by post-deposition annealing at different temperatures. Simulated patterns generated using LEEDPat highlight the diffraction spots associated with the different structural arrangements. Yellow circles and the overlaid unit cell for each LEED pattern correspond to the Au(111) substrate. (a) The Rec(7.7 × 3.85) reconstruction associated with the X-phase obtained after deposition of approximately 0.66 ML Sn, with colored dots marking the three unique sub-patterns corresponding to different rotational domains. **(b)** LEED pattern of the striped phase. **(c)** The three unique sub-patterns of the $\begin{pmatrix} 2 & 1 \\ 1 & 3 \end{pmatrix}$ reconstruction (also referred to as the $\sqrt{7}$-reconstruction) are marked with colored circles. **(d)** The unit cell and $(\sqrt{3} \times \sqrt{3})$R30° pattern of the Au_2Sn surface alloy are indicated in blue.

A step-by-step preparation is possible: annealing the X-phase first to approximately 450 K forms the striped phase, which can then be transformed into the $\sqrt{7}$-phase by subsequent heating to slightly higher temperatures.

Each structural phase can also be formed by depositing only the corresponding Sn thickness indicated in Figure 1. Without any post-deposition annealing, a mixture of phases often results, as shown in the Supporting Figure S4 for a mixed $\sqrt{7}/Au_2Sn$ phase. A mixture of structural phases involving the striped phase was rarely observed, which might be due to the small parameter window, in post-deposition annealing temperature, as well as in the Sn coverage, in which the striped phase forms. We note, however, that the LEED pattern presented by Maniraj et al. for annealing the X-phase to 450 K, which they named Mix phase, seems to be a mix between the X-phase and the striped phase [22]. In general, the preparation of both the striped phase and the $\sqrt{7}$-phase is challenging due to their high sensitivity to the Sn coverage. This sensitivity is, in fact, the reason for the narrow post-deposition annealing window: the structural phase is dictated by the Sn film thickness, which is best controlled by thermal desorption. Likely, Sn atoms can rearrange and form totally different stable structural phases, depending on the Sn coverage. While the direct deposition of the exact coverage for each phase on the Au(111) surface, kept at room temperature, actually leads to the formation of the desired structural phase, we noted that this often results in poorer long-range order. We therefore found that controlling the Sn coverage by post-deposition annealing provides a more reliable method for preparing well-ordered structural phases. In addition, the controlled Sn desorption via post-deposition annealing allowed for monitoring the structural transitions in parallel via LEED, which, as the parameter window for preparing the striped and $\sqrt{7}$-phase is small, allowed for precisely observing the parameters at which the structural transitions happen.

We recorded XPS survey spectra to assess the chemical composition across the different structural phases and to quantify the Sn coverage after thermally driven Sn-desorption during post-deposition annealing.

In Figure 2 spectra recorded with a photon energy of $h\nu = 700$ eV at an emission angle of $\Theta = 60°$ are shown. The bottom spectrum represents the X-phase, with spectra of the other structural phases stacked above.

No contamination was detected; characteristic signals of common contaminants such as C 1s and O 1s are absent, as highlighted by red boxes in Figure 2. With increasing annealing temperature, Sn-related features, especially the Sn 3d doublet at $E_{\mathrm{bin},Sn\,3d} \approx 490$ eV and the Sn 4d peak at $E_{\mathrm{bin},Sn\,4d} \approx 24$ eV, decrease, reflecting thermally driven desorption of Sn atoms.

The Sn coverage was estimated from XPS survey spectra, yielding coverages of 0.63(5) ML for the X-phase and 0.33(3) ML for the Au_2Sn-alloy, in good agreement with quartz crystal microbalance measurements of 0.66(2) ML and 0.33(2) ML, respectively. In contrast, the striped and $\sqrt{7}$ phases were obtained by post-deposition annealing of the X-phase and thus cannot be quantified by quartz crystal measurements. From XPS, their coverages were determined as 0.55(2) ML and 0.46(3) ML, respectively.

To complement the coverage analysis, we next turn to the chemical evolution of the Sn 4d core-level spectra shown in Figure 3, with detailed fit parameters summarized in Table 1. We

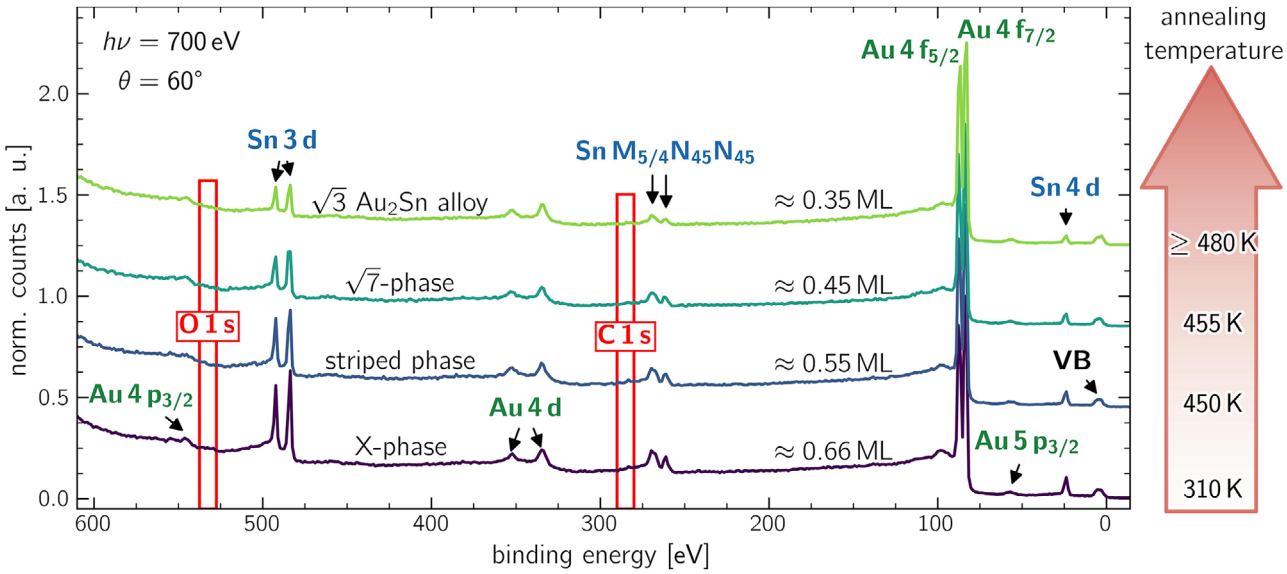

FIGURE 2 | XPS survey spectra of the Sn phases obtained after deposition of 0.66 ML Sn at room temperature, followed by post-deposition annealing at different temperatures. All spectra were recorded using a photon energy of $h\nu = 700$ eV and an emission angle of $\Theta = 60°$. Binding energies are referenced to the Fermi level. The survey spectra reveal the desorption of Sn during the annealing process.

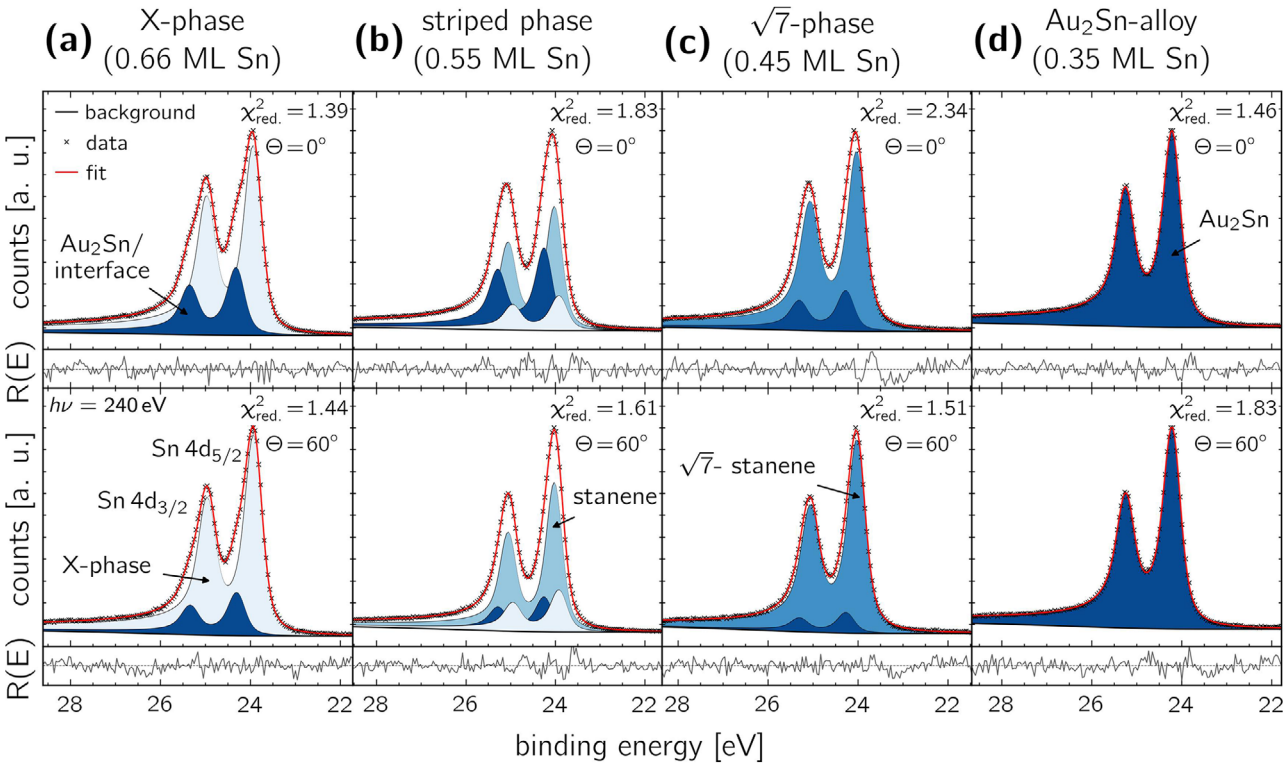

FIGURE 3 | High-resolution XPS spectra of the Sn 4d core level, used to investigate the internal chemical composition of the topmost Sn layer(s). Spectra were recorded at a photon energy of $h\nu = 240$ eV with emission angles of $\Theta = 0°$ (top row) and $\Theta = 60°$ (bottom row). The corresponding fit parameters are listed in Table 1.

begin with the X-phase in Figure 1(a). The best fit is achieved using two components. The component plotted in dark blue at $E_{bin} \approx 24.29$ eV, is assigned to the Au_2Sn-alloy. The second component, plotted in white at $E_{bin} \approx 23.92$ eV, is assigned to Sn atoms in the square-like arrangement of the X-phase located in the topmost layer. We observe that the intensity of the component plotted in white increases under surface-sensitive conditions at $\Theta = 60°$. For a detailed discussion of the structural model of the X-phase, we refer to our recent publication [23].

The spectrum of the striped phase, shown in Figure 3b, is best fitted using three components. Two match the Au_2Sn alloy

TABLE 1 | Fit parameters from the XPS analysis of the chemical evolution of the Sn 4d signal shown in Figure 4. The statistical fit error for the reported binding energies is typically well below 10 meV.

Structural phase	Θ [°]	Component	E_{bin} [eV]	E_{SOC} [eV]	FWHM [eV]	asymmetry β	rel. area [%]
X-phase Figure 4a	0	X-Phase	23.92	1.04	0.48	0.12	73.88
		Au_2Sn	24.29	1.04	0.48	0.12	26.12
	60	X-Phase	23.91	1.04	0.48	0.12	82.39
		Au_2Sn	24.28	1.04	0.48	0.12	17.61
striped phase Figure 4b	0	X-Phase	23.92	1.04	0.47	0.12	15.44
		Au_2Sn	24.25	1.04	0.47	0.12	36.10
		stanene	24.02	1.04	0.44	0.09	48.46
	60	X-Phase	23.91	1.03	0.47	0.12	20.16
		Au_2Sn	24.25	1.03	0.47	0.12	16.60
		stanene	24.02	1.03	0.44	0.09	63.25
$\sqrt{7}$ phase Figure 4c	0	Au_2Sn	24.25	1.04	0.47	0.12	18.03
		$\sqrt{7}$-stanene	24.01	1.04	0.49	0.10	81.97
	60	Au_2Sn	24.25	1.03	0.47	0.11	9.67
		$\sqrt{7}$-stanene	24.01	1.03	0.48	0.09	90.33
Au_2Sn-alloy Figure 4d	0	Au_2Sn	24.19	1.04	0.49	0.11	100.00
	60	Au_2Sn	24.19	1.03	0.49	0.11	100.00

and the square-like X-phase components discussed above. The spectrum is dominated by a third component, plotted in light blue at $E_{bin} \approx 24.02$ eV, which we identify as a stanene arrangement in accordance with our structural analysis below. Here, the stanene-related core-level signal exhibits a shift of about 230 meV towards lower binding energies relative to the alloy component. For comparison, a somewhat smaller shift of ~170 meV between the stanene and the alloy component was reported for atomically flat honeycomb stanene grown on an Ag_2Sn-alloy on Ag(111) [26]. We note that this binding energy ordering, with the alloy component at a higher binding energy (≈ 24.29 eV) than the 2D stanene layer (≈ 24.02 eV), is the opposite of the behaviour observed in similar sample systems like silicene and germanene on Ag(111) [27, 28], where the binding energy of the alloy component is lower than the 2D layer component. A simple model based on Pauling electronegativity (Au: 2.54 vs. Sn: 1.96) would predict a Sn → Au charge transfer, which should increase the binding energy of the Sn 4d alloy component but should decrease the Au 4f alloy components binding energy. However, as discussed below in the analysis of the Au 4f signal, *both* the Sn 4d and Au 4f alloy components shift to higher binding energies. As Egelhoff demonstrated, the reason for the observed component shifting is not explained by simple charge transfer but a complex interplay of final-state effects and initial-state intra-atomic rehybridization (e.g., Au 5d → 6s) upon alloying [29]. This anomalous component shifting behaviour is not only well-known for Au-Sn, but known for Ag-Sn alloys as well [30–32].

Most notably, the stanene component exhibits a significantly reduced asymmetry of $\beta = 0.09$ and a narrower full width at half maximum (FWHM) compared to the other components. All spectra were recorded under identical conditions, including photon energy, room temperature, and spectrometer settings. Therefore, Gaussian broadening contributions, such as instrumental, thermal, and source-related effects, are expected to remain constant across all measurements. Thus, the observed FWHM reduction likely stems from an increased core-hole lifetime, which suggests a less metallic character [33, 34] and points to predominant sp^2 bonding rather than the sp^2/sp^3 hybridization predicted by theory for freestanding, buckled stanene [1]. Our STM measurements confirm an atomically flat honeycomb structure, indicating that sp^2 bonding is strongly favored due to the lack of detectable buckling. The measured binding energy of the stanene component, $E_{bin} \approx 24.02$ eV, closely matches literature values for bulk tin, $E_{bin} \approx 23.9$ eV to 24.0 eV [35, 36].

The ratio of the stanene component area to that of the X-phase remains roughly constant at 3.1:1 across both emission angles. Due to their similar angular dependence, we conclude that the corresponding Sn atoms are located within the same atomic layer. In contrast, the Au_2Sn-alloy component exhibits an angular dependence, with higher intensity at normal emission, consistent with its location beneath the topmost layer. Using our atomically resolved STM images as presented in Section 2.1, we identified 34 Sn atoms in the top layer of the $\mathrm{Rec}(16 \times 2\sqrt{3})$ unit cell: 8 atoms form a square-like configuration similar to the X-phase, while 26 atoms are arranged in a honeycomb structure. This atomic ratio of 3.25:1 (26:8) is in excellent agreement with the measured XPS area ratio of 3.1:1. This quantitative agreement is discussed in detail in Section 2.1 when presenting the full structural model.

For the $\sqrt{7}$-phase, a fit including two components gives the best result. We still identify a Au_2Sn-alloy component; the X-phase component, however, is no longer detected. At the surface-sensitive grazing angle of $\Theta = 60°$, the spectrum is dominated by

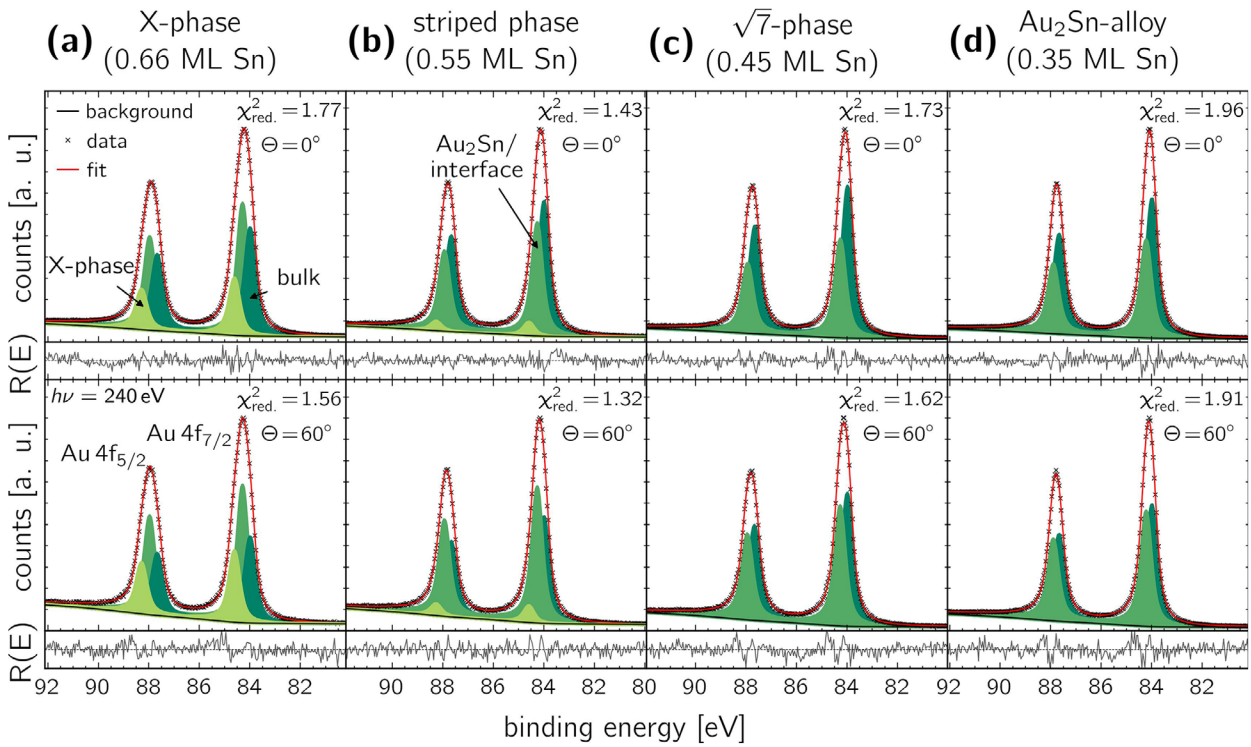

FIGURE 4 | High-resolution XPS spectra of the Au 4f core level used to analyze the interface structure of the different Sn phases. Spectra were acquired at a photon energy of $h\nu = 240$ eV with emission angles of $\Theta = 0°$ (top row) and $\Theta = 60°$ (bottom row). Fit parameters corresponding to these spectra are provided in Table 2.

a single component. Its binding energy is similar to the stanene component of the striped phase. We nevertheless plotted it in a different shade of blue to distinguish the stretched honeycomb Sn-dimer arrangement reported by Maniraj et al. [22] from the honeycomb stanene arrangement observed in the striped phase. STM measurements for this phase (Figure S2, Supporting Information) show that the two Sn atoms forming a dimer occupy nearly equivalent substrate sites, explaining the single chemical environment observed in the XPS spectra.

Remarkably, the binding energies of stanene in the striped phase and the $\sqrt{7}$-stanene are nearly identical and cannot be distinguished based solely on XPS data. Complementary structural analysis using LEED and STM, however, confirms that these are distinct structural phases. Comparing the structural models of the striped phase (Section 2.1) and the $\sqrt{7}$-stanene proposed by Maniraj et al. [22], structural similarities are identified. Only a small lateral displacement of neighboring Sn atoms of the honeycomb stanene is needed to form Sn-dimers on a stretched hexagonal lattice. This subtle structural change is consistent with (i) the very narrow range of Sn coverages and annealing conditions required to prepare either phase, (ii) the nearly identical shape and fit of the Au 4f core-level spectra (compare panels (b) and (c) in Figure 4, ignoring the X-phase contribution in the striped phase), and (iii) the near-identical binding energies of the stanene-related component in the Sn 4d spectra.

Similar to the honeycomb stanene of the striped phase, the $\sqrt{7}$-stanene component shows a reduced asymmetry as the honeycomb stanene in the striped phase, which we again assign to sp^2-like bonding [35]. Its FWHM is slightly broader, which may reflect the somewhat different local environments of the two Sn atoms within the dimer, caused by the small buckling observed [22]. The measured broader FWHM could also indicate increased structural disorder, similar to the ordered–disordered phase reported for germanene on Ag(111) [28, 37–40]. Indeed, our STM data of the $\sqrt{7}$-phase, as shown in the Supporting Information in Figure S3, reveal regions where hexagonal stanene and stretched Sn-dimer structures coexist, supporting this interpretation.

The second component, plotted in dark blue, is attributed to the Au_2Sn-alloy. Given its low intensity and the very small parameter window needed for the preparation of the $\sqrt{7}$-phase, we propose two possible origins: either residual Au_2Sn-alloy in regions that did not fully underwent the structural transition from the striped to the $\sqrt{7}$-phase, or realloying towards the Au_2Sn-alloy phase has already begun. Both explanations seem plausible considering the narrow preparation window in which the $\sqrt{7}$-phase forms.

Finally, for the Au_2Sn-alloy phase, shown in Figure 3d, the spectrum is well described by a single component assigned to Sn atoms in the Au_2Sn-alloy. The fit parameters derived for the Au_2Sn phase, obtained by Sn desorption after annealing the X-phase to 650 K, are in excellent agreement with those obtained for the alloy after depositing 0.33 ML Sn on bare Au(111) at room temperature [20, 24, 41].

We analysed the interfacial chemical evolution using Au 4f core-level spectra. Starting with the spectra of the X-phase shown in

TABLE 2 | XPS analysis fit parameters to the chemical evolution of the Au 4f signal shown in Figure 3. The statistical fit error for the reported binding energies is typically well below 10 meV.

Structural phase	Θ [°]	Component	E_{bin} [eV]	E_{SOC} [eV]	FWHM [eV]	asymmetry β	rel. area (%)
X-phase Figure 3a	0	bulk	84.00	3.68	0.54	0.03	36.32
		interface	84.30	3.68	0.54	0.03	44.40
		X-phase	84.62	3.68	0.54	0.03	19.28
	60	bulk	84.00	3.68	0.54	0.03	29.24
		interface	84.30	3.68	0.54	0.03	46.54
		X-phase	84.62	3.68	0.54	0.03	24.22
striped phase Figure 3b	0	bulk	84.00	3.67	0.53	0.03	51.49
		interface	84.27	3.67	0.53	0.03	43.26
		X-Phase	84.59	3.67	0.53	0.03	5.25
	60	bulk	84.00	3.67	0.53	0.04	41.05
		interface	84.27	3.67	0.53	0.04	52.42
		X-Phase	84.59	3.67	0.53	0.04	6.53
$\sqrt{7}$ phase Figure 3c	0	bulk	83.99	3.67	0.54	0.03	60.61
		interface	84.27	3.67	0.54	0.03	39.39
	60	bulk	84.00	3.67	0.54	0.03	52.53
		interface	84.28	3.67	0.54	0.03	47.47
Au_2Sn-alloy Figure 3d	0	bulk	84.00	3.68	0.54	0.03	58.66
		Au_2Sn	84.23	3.68	0.54	0.03	41.34
	60	bulk	84.00	3.68	0.53	0.03	51.31
		Au_2Sn	84.23	3.68	0.53	0.03	48.69

Figure 4a, we identify three components. The bulk contribution, plotted in dark green, is found at a binding energy of E_{bin} = 84.00 eV. The most intense feature is shifted by approximately 300 meV to higher binding energy and is attributed to the Au_2Sn interface layer. A third component, located at E_{bin} = 84.62 eV, is assigned to the X-phase.

The observed angular dependence of the components matches the expected stacking order. The bulk signal decreases at the more surface-sensitive emission angle of Θ = 60°. Meanwhile, the X-phase component increases, indicating that the X-phase forms at the surface, on top of the Au_2Sn interface layer. Detailed fit parameters are summarized in Table 2. The slight asymmetry of $\beta = 0.03$, observed for all components, is typical for noble metal core levels due to many-body final-state effects [35, 42], and the bulk binding energy is in excellent agreement with the literature [43]. A detailed discussion of the structural model of the X-phase is provided in our recent publication [23].

Proceeding to the striped phase, shown in Figure 4b, the same components are observed, but with altered relative intensities and slight shifts in binding energy. Both the X-phase and Au_2Sn interface components shift by approximately 30 meV toward lower binding energy. The X-phase component intensity significantly decreases, consistent with desorption or rearrangement of Sn atoms formerly arranged in the X-phase configuration. In contrast to the X-phase spectrum, the Au_2Sn interface component now shows a stronger angular dependence, indicating a reduced overlayer thickness in this phase. These changes point to a restructuring process in which the striped phase forms at the expense of the X-phase. This is in line with the Sn 4d core-level fits discussed above and matches our structural model discussed below in Section 2.1. We propose that a dealloying process of the Sn atoms occurs during the structural transition from the X-phase to the striped phase. In the X-phase, Sn atoms arranged in a square-like pattern grow atop an Au_2Sn-alloy, whereas in the striped phase, the honeycomb-arranged Sn grows directly on the Au(111) substrate without forming an interface alloy. Meanwhile, the square-like regions within the stripes likely remain positioned on Au_2Sn-stripes incorporated into the topmost substrate layer. This proposed dealloying scenario is further supported by the packing density of the Sn atoms, which is higher in the honeycomb arrangement of the striped phase than in the square-like layer of the X-phase. Considering that the overall Sn coverage decreases during post-deposition annealing, the surplus Sn needed to form the striped phase with higher packing density likely originates from the dealloying of the interface Au_2Sn-alloy in the X-phase.

Further annealing results in the formation of the $\sqrt{7}$-phase, for which the fit consists of only two components: the bulk and the Au_2Sn interface contributions. The interface component remains bound at $E_{bin} \approx 84.27$ eV, as previously observed for the striped phase, and continues to exhibit strong angular dependence, further supporting its location beneath the stanene-like top layer.

Finally, annealing the sample above 480 K results in the formation of the Au_2Sn-alloy phase. The Au 4f spectra in this regime are best described by a two-component model, similar to the $\sqrt{7}$-phase: a bulk contribution and a second component located at a slightly smaller binding energy of $E_{bin} \approx 84.23$ eV in comparison to the spectra of the $\sqrt{7}$-phase, which we assign to the Au_2Sn-alloy. This component is slightly shifted toward lower binding energies compared to the interface component identified in the preceding phases. As with our Au_2Sn Sn 4d core-level fits, the results agree well with earlier reports of Au_2Sn alloy formation on Au(111) after deposition of ≈ 0.33 ML Sn at room temperature [20, 24, 41].

LEED measurements reveal a $(\sqrt{3} \times \sqrt{3})R30°$ reconstruction, characteristic of the Au_2Sn-alloy, once the annealing temperature exceeds 480 K. This LEED pattern remains stable up to ≈ 900 K, at which point it vanishes. Interestingly, even though the LEED signal remains unchanged, we observe subtle but continuous changes in the XPS spectra of both Au 4f and Sn 4d core levels across this temperature window.

The Au 4f spectra show a gradual shift of the Au_2Sn/interface component from $E_{bin} \approx 84.27$ eV towards lower binding energies with increasing annealing temperature. For the spectrum presented in Figure 4d at a post-deposition annealing temperature of 650 K, the binding energy is found to be $E_{bin} = 84.23$ eV. Above this annealing temperature, no residual Sn component, besides the Au_2Sn component, is detectable in the Sn 4d spectra. Further annealing to ≈ 750 K lowers the binding energy to around $E_{bin} \approx 84.20$ eV, consistent with the value observed for the Au_2Sn-alloy prepared by depositing ≈ 0.33 ML of Sn on bare Au(111) at room temperature. These results are in excellent agreement with previous reports [20, 24, 41]. We note that, within annealing in this temperature range, the decrease of Sn coverage is negligible.

We propose that the interface component observed in all the other discussed structural phases and the Au_2Sn-alloy component of the Au_2Sn-phase exhibit similar binding energies due to comparable local environments. In the Au_2Sn-alloy, the atomic ratio of Au:Sn in the Au_2Sn-layer is 2:1. For the striped and $\sqrt{7}$ phases, the Sn coverage yields a similar local elemental composition compared to an Au_2Sn alloy for Au atoms located at the interface of the Au bulk and the Sn overlayer, suggesting that the Sn overlayer could induce binding energy shifts in the topmost Au atoms similar to those in the alloyed configuration. Notably, the interface component of all the structural phases discussed in our XPS analysis is shifted to slightly higher binding energies in comparison to the binding energy of the Au_2Sn-alloy component in the Au_2Sn-alloy phase.

The continuous shift of the Au_2Sn component observed for the Au_2Sn-alloy phase toward lower binding energies with increasing annealing temperature suggests that some residual Sn atoms likely remain bound to the surface even after the Au_2Sn-alloy formation begins. Likely, only upon annealing at sufficiently high temperatures, the desorption of dimer-like $\sqrt{7}$ Sn completes and yields the final Au_2Sn-alloy phase.

Taking into account both our Au 4f core-level fits and the Sn 4d analysis, we conclude that after the initial dealloying of Sn atoms from the X-phase to the $\sqrt{7}$-phase, realloying occurs with increasing annealing temperature, leading to the formation of Au_2Sn at temperatures above 480 K. Our XPS results indicate that with further annealing, the Sn-dimer bonds of the $\sqrt{7}$-phase break and the atoms begin to form the Au_2Sn-alloy again, for which all experimental measurements, LEED, XPS, and STM are in perfect agreement to the Au_2Sn-alloy obtained after the deposition of ≈ 0.35 ML Sn on bare Au(111) at room temperature.

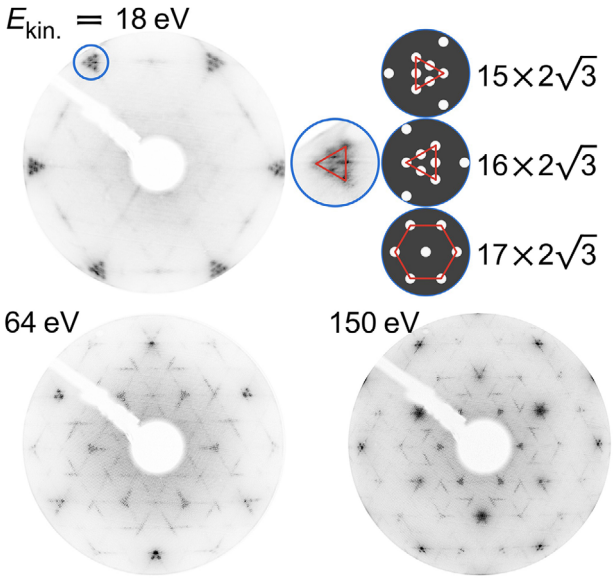

FIGURE 5 | Structural analysis of the striped phase using LEED. LEED patterns recorded at different kinetic energies show a triangular and striped-like pattern. Analysis of the substructure in the LEED pattern recorded at $E_{kin.} = 18$ eV reveals a $Rec(16 \times 2\sqrt{3})$ supercell.

Alternatively, the sequence of structural transitions can also be explained in terms of Sn coverage. Starting from the Au_2Sn-alloy at ≈ 0.35 ML, a slight increase in coverage to ≈ 0.45 ML drives dealloying and the formation of Sn dimers in the $\sqrt{7}$-phase. Further increase in coverage initiates two-layer growth in the striped phase, where honeycomb stanene stripes on the bare Au(111) surface coexist with square-like stripes grown atop Au_2Sn. At ≈ 0.66 ML, corresponding to the X-phase, the Au_2Sn alloy layer is reformed with a square-like Sn overlayer atop.

In addition to this core-level analysis, we also investigated the valence band evolution across the structural phases. These valence band spectra, are presented and discussed in the Supporting Information (Section S4, Figure 5).

2.1 | STM and Structural Model of the Striped Phase

After discussing the structural evolution of the different Sn phases, we now focus on the structural analysis of solely the striped phase.

The periodicity of the striped LEED pattern was determined first. In Figure 5, LEED patterns recorded at different kinetic energies are shown. A clear spot-superstructure, in addition to the stripe-like and triangular features observed, is visible in the

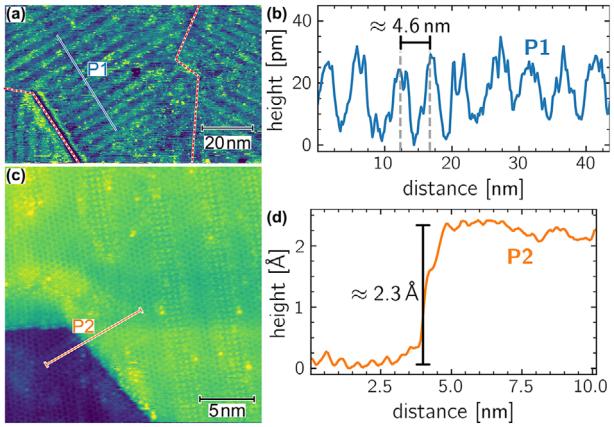

FIGURE 6 | STM analysis of the striped phase. (a) Large-scale STM image measured at $U = 4\,\text{mV}$ and $I = 310\,\text{pA}$, displaying alternating stripes of square-like and honeycomb arrangements of Sn atoms. The dashed red lines mark the borders of the three rotational domains. (b) Line profile along the path shown in (a). The average distance between neighboring stripes is approximately 4.8 nm. (c) Step edge of the striped phase measured at $U = 3\,\text{mV}$ and $I = 400\,\text{pA}$. To visualize the atomic structure on both terraces, the same STM image is shown in the Supporting Information (Figure S6) with adapted color scaling. (d) Line profile corresponding to the step edge in (c).

pattern. By measuring the distances of these superstructure spots relative to the Au(111) substrate spots, we extract an average periodicity of 16.2(8) along the $[1\bar{1}0]$ direction and $3.5(2) \approx 2 \times \sqrt{3}$ along $[11\bar{2}]$. To verify this periodicity, we examined the superstructure surrounding the $\sqrt{3}$-spot in the LEED pattern recorded at $E_{\text{kin.}} = 18\,\text{eV}$ (inset of Figure 5). Comparing the experimental LEED patterns with simulated superstructures generated using LEEDPAT [44] shows that only the Rec$(16 \times 2\sqrt{3})$ periodicity reproduces the observed spot arrangement. Especially the characteristic features of the experimental pattern, such as the inward-pointing triangular shape of the superstructure, match well, while simulating the Rec$(15 \times 2\sqrt{3})$ produces a triangle pointing outward, and Rec$(17 \times 2\sqrt{3})$ results in a hexagonal configuration inconsistent with the measurements.

For a Rec$(13 \times 2\sqrt{3})$ and a Rec$(19 \times 2\sqrt{3})$ periodicity, the reflex patterns would also be an inward-pointing triangular reflex pattern. The corresponding spot distances, however, are inconsistent with our experimental data. Thus, we confidently assign the observed striped LEED pattern to a Rec$(16 \times 2\sqrt{3})$ supercell.

We now turn to the STM analysis of the striped phase, focusing first on its long-range order and step height.

In the large-scale STM image of the striped phase in Figure 6(a), alternating bright and dark stripes with three rotational domains, with their borders marked by the dashed red lines, are observed. One domain is visible on the right-hand side of the image, another occupies the center and extends to the left, and a third domain appears below the dark defect in the lower-left corner. The three domains are rotated by 120° with respect to one another, consistent with the threefold symmetry of the underlying Au(111) substrate. The longest region of stripes, before ending at a domain border, defect, or step edge, that we observed measured approximately ≈ 120 nm in length.

To quantify the periodicity of the stripes, we analyzed 27 line profiles across the stripes, similar to the one shown in Figure 6b. We extract an average stripe distance of 4.6(4) nm, which corresponds to a 16.1±1.5-fold multiple of the Au lattice constant $a_{\text{Au}} = 2.88$ Å. This is in excellent agreement with the periodicity determined from our LEED measurements.

An STM image of an atomic step edge in the striped phase is shown in Figure 6c. In the Supporting Information (see Figure S6), we provide the same STM image with an adjusted color scale to resolve atomic resolution on both terraces. The corresponding line profile in Figure 6d confirms that the striped phase follows the underlying substrate morphology. We measured a step height of ≈ 2.3 Å, in agreement with the height of a monoatomic step on clean Au(111) [45, 46]. STM images in Figure 6 demonstrate that the striped phase can grow uniformly on terraces and that the striped arrangement begins directly at the step edges, confirming the large-area growth of this structure.

To determine the atomic arrangement in the unit cell, we present an atomically resolved STM image of the striped phase in Figure 7a. The corresponding marked line profiles are shown in Figure 7b.

Line profile **P1**, taken across both regions, shows that the striped phase is atomically flat. A slight height difference of about 20 pm is observed between the square-like and honeycomb stripes. We observed that this contrast can vanish or even reverse, as in Figure 6a, where the square-like region appears lower. The observed slight height variation is likely caused by the STM tip state and not an actual height difference between the two regions.

Line profile **P2** of the honeycomb region shows an atomically flat arrangement with a nearest-neighbor distance of ≈ 2.9 Å, which matches the Au(111) lattice constant. The distance of two minima in the profile is ≈ 8.6 Å, which equals $3a_{\text{Au}}$. Therefore, the diagonal of the honeycomb hexagon matches $2a_{\text{Au}}$. The honeycomb Sn lattice therefore matches the Au(111) lattice and Sn atoms occupy equivalent adsorption sites on the Au(111) substrate, consistent with previous reports on the $\sqrt{7}$-phase [22] and with DFT results [17].

Line profile **P3** of the square-like region shows an atomically flat arrangement with minimal height variation. The nearest-neighbor distance of ≈ 5 Å corresponds to a $\sqrt{3}$ periodicity relative to the Au(111) substrate, allowing all Sn atoms in the square-like region to occupy hcp hollow sites. The square-like arrangement in the striped phase closely resembles that of the X-phase in both lattice constant and geometry, with the lattice constant being approximately 10% smaller than observed in the X-phase. Considering the chemical similarities observed in their XPS spectra, it is likely that these two square-like arrangements are closely related [23].

Using atomically resolved STM images of the striped phase, as shown in Figure 7a and 7c, together with larger-scale images such as Figure 6a, we measured a total of 108 individual

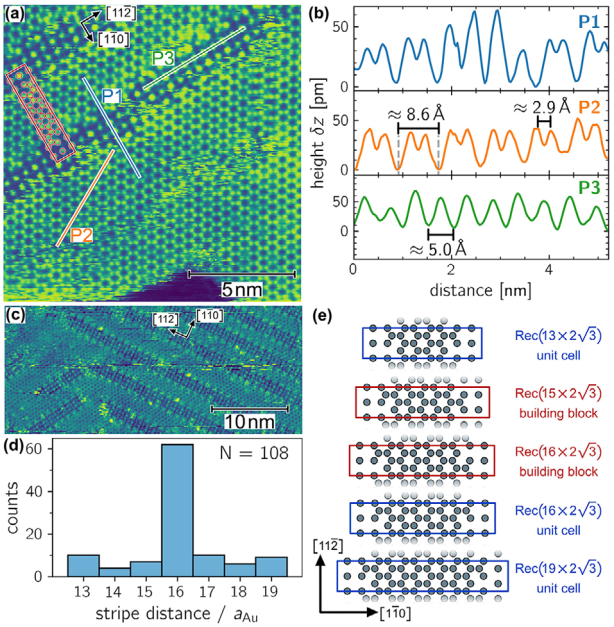

FIGURE 7 | High-resolution STM analysis of the striped phase: a) Atomically resolved STM image showing an atomically flat honeycomb arrangement of Sn atoms, separated by Sn atoms in a square-like arrangement. A Rec($16 \times 2\sqrt{3}$) building block is overlaid in red. The image was acquired at $U = 3$ mV and $I = 360$ pA. b) Line profiles corresponding to the marked lines in (a). Profile **P1** indicates that the square-like stripe is slightly elevated relative to the honeycomb region. c) High-resolution image of the striped structure showing a slight variation in the width of the honeycomb stripe. The image was acquired using the same parameters as in (a). d) Distribution of the periodicity length, measured as the distance between the centers of the square-like stripes and determined from seven different STM images. e) Examples of building blocks and unit cells identified in the high-resolution STM images, with the Rec($16 \times 2\sqrt{3}$) building block and unit cell being the most common motif.

distances between neighbouring stripes. Shown in Figure 7d is the distribution of distances, in units of the Au(111) lattice constant. Most frequently, we observed a $16 \cdot a_{Au}$ distance between stripes. Distances ranging from $13 \cdot a_{Au}$ to $19 \cdot a_{Au}$, are also observed. This translates to widths of the honeycomb-stripes ranging from ≈1.5 nm to ≈ 3.2 nm, with the honeycomb-stripe width of ≈ 2.4 nm being the most commonly observed.

In our atomically resolved STM images, we can clarify the nature of the striped phase. The structure consists of two alternating components: (1) square-like stripes and (2) honeycomb stanene nanoribbons. The square-like stripes have a fixed width of ≈ 14.6 Å. In contrast, the honeycomb nanoribbons have a variable width, resulting in different cell sizes as shown in Figure 7e.

To clarify our terminology, we distinguish these cells based on their symmetry. We define *unit cells* (outlined in blue in Figure 7e) as a motif that possesses a mirror symmetry plane parallel to the [11$\bar{2}$] axis. We define *building blocks* (outlined in red) as a small variation of the unit cell that lacks this mirror symmetry. We illustrate the difference between the building blocks and unit cells in detail in the Supporting Information (Figure S6). The mirror symmetry of the unit cells is broken by a single Sn atom at the

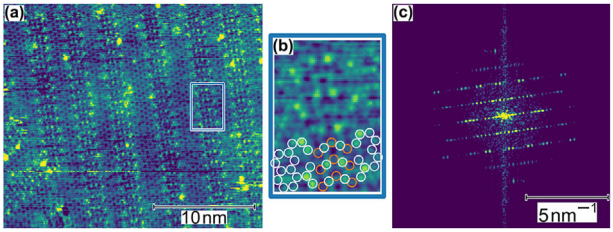

FIGURE 8 | High-resolution STM image of the striped phase, acquired with a slightly different tip-state compared to the other STM images, revealing indications of atoms in the layer beneath the topmost layer. a) Image measured at $U = 3$ mV and $I = 290$ pA. b) Zoom-in of the region marked in (a), revealing a subtle substructure beneath the atoms in the topmost layer of the square-like stripe. Locations expected for an Au_2Sn-alloy layer below the square-like lattice are marked with orange circles, while the atoms in the striped top layer are marked in white. c) Fast-Fourier transform (FFT) of the STM image in (a), showing excellent agreement with a single domain of the LEED pattern of the striped phase.

honeycomb-square border in a triangular planar site shifting by $\sqrt{3}a_{au}$ to an adjacent, equivalent site along the [11$\bar{2}$] direction.

Our distinction is important because the square-like region exhibits identical mirror symmetry parallel to the [11$\bar{2}$] axis, as do the cells classified as unit cells. Therefore, solely using one type of building block cannot tile the surface to build the observed structure. However, the difference between the building blocks and unit cells is only the position of a single atom, and we observe a lack of perfect long-range order in the system, as the majority of the surface consists of a mixture of mirror-symmetric unit cells and building blocks that lack mirror symmetry. The Rec($16 \times 2\sqrt{3}$) periodicity is simply the most common.

Finally, we also note that this striped superstructure is a long-range phenomenon. As shown in the Supporting Information (Figure S7), the striped pattern often fails to form near surface distortions, such as step edges or islands. In these regions, we instead observe larger, but usually distorted honeycomb stanene areas.

For reference, we marked a Rec($16 \times 2\sqrt{3}$) building block in the STM image in Figure 7a in red.

Figure 8c shows the Fast-Fourier Transform (FFT) of the STM image in Figure 8a. The stripe-like, spot-rich pattern matches well with the features of a single-domain LEED pattern as shown in Figure 5.

Based on our LEED analysis, which identifies a Rec($16 \times 2\sqrt{3}$) unit cell, and our STM results, which further confirm this cell as the most frequently observed, together with our XPS data, we propose the structural model shown in Figure 9. In this model, the honeycomb-like region forms directly on the Au(111) surface, with the Sn atoms occupying equivalent hcp hollow sites, consistent with DFT predictions [17].

In analogy with the X-phase, we propose that the square-like stripe regions grow on top of an Au_2Sn-alloy layer. Several

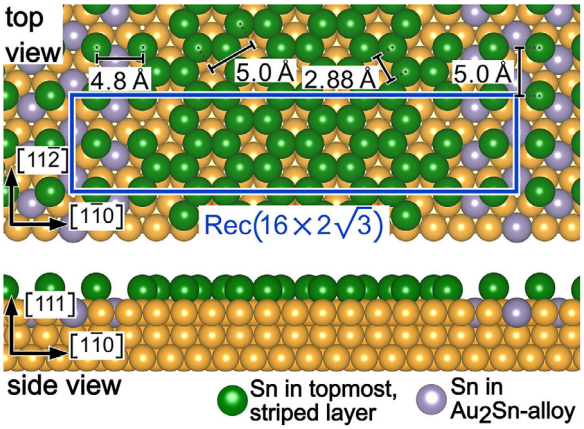

FIGURE 9 | Proposed structural model of the Rec($16 \times 2\sqrt{3}$) Sn honeycomb striped phase. Sn atoms in the topmost layer are shown in green, while the other Sn atoms, arranged in the Au_2Sn-alloy configuration beneath the square-like ordered Sn atoms in the separation region, are shown in grey.

observations support this interpretation: (i) Counting the Sn atoms visible in the topmost layer from STM images does result in smaller coverages in comparison to the coverages we determined by XPS. The two values differ approximately by the same number of atoms as those forming the square-like arrangement in the topmost layer. This density matches the atomic density needed to form a stripe of Au_2Sn-alloy beyond the square-like region. (ii) Our chemical analysis of the structural evolution reveals very similar Au 4f and Sn 4d contributions for the X-phase and the striped phase. The Sn 4d spectrum for the striped phase (see Table 1) shows two distinct topmost-layer components, which we attribute to the honeycomb (stanene) and square-like (X-phase) arrangements. The measured intensity ratio of these components is 3.1:1 (stanene:square-like Sn). This is in excellent agreement with the atomic ratio derived from our STM-based structural model (Section 2.1), which features 26 stanene atoms and 8 square-like arranged atoms per unit cell. This yields an atomic ratio of 3.25:1 (26:8), which supports our XPS component assignment and the proposed structural model.

(iii) According to our XPS analysis, a dealloying process happens with increasing annealing temperature and therefore decreasing Sn coverage. Starting with the X-phase, with a square-like Sn overlayer growing atop an Au_2Sn alloy layer, and ending with the $\sqrt{7}$ phase of a Sn-dimer layer grown directly on Au(111) without alloying. The striped phase in between would then be interpreted as a partially dealloyed configuration. (iv) As shown in the inset of Figure 8b, depending on the STM tip state, we can resolve the substructure in the square-like region. By white circles, the atomic positions of Sn atoms in the topmost layer and by orange circles the expected locations of Sn atoms in the underlying alloy layer are marked in the inset. This assignment closely resembles the observed substructure.

Considering the distinct structural and chemical characteristics of the square-like and honeycomb-like regions, our observations might be interpreted as stanene zigzag nanoribbons.

In summary, we provide the first evidence of ultraflat regular honeycomb stanene on Au(111). In addition, our results mark the first report of a distinct striped Sn arrangement. The striped phase could be interpreted as stanene nanoribbons in the zigzag configuration. Our results confirm the remarkable structural versatility of Sn on Au(111), especially the high sensitivity of the structural phases to subtle variations of the preparation parameters, similar to the structural diversity observed for Si on Ag(111) [47–49].

We observed that the Au_2Sn surface alloy stabilizes different complex structural arrangements of Sn in the topmost layer. The square-like X-phase, which forms on a complete Au_2Sn layer, undergoes dealloying toward the $\sqrt{7}$ stretched honeycomb phase that grows directly on bare Au(111), with the structural transition driven by the desorption of Sn, which is controlled by the post-deposition annealing temperature. The striped phase, observed in between, is a mixed phase with a very complex structural arrangement, where the regular honeycomb stanene nanostripes are likely stabilized by the square-like Sn stripes growing atop a Au_2Sn-alloy region. When the annealing sufficiently reduces the Sn coverage, realloying occurs. The $\sqrt{7}$-phase transforms back into a Au_2Sn surface alloy exhibiting a $(\sqrt{3} \times \sqrt{3})$R30° reconstruction, similar to the Au_2Sn alloy formed by depositing ≈ 0.35 ML of Sn on Au(111) at room temperature. It appears likely that the alternating arrangement of honeycomb and square-like Sn is stabilized by the coexistence of bare Au(111) and Au_2Sn regions at the substrate surface. The complex structure of the striped phase may self-stabilize through substrate–adsorbate interactions, similar to the reported ground state of germanene on Ag(111) in a $Ge_{98}Ag_6$ ($\sqrt{109} \times \sqrt{109}$)R24.5° supercell [50] and the formation of atomically flat plumbene on a $Pd_{(1-x)}Pb_x$ foam-like bubble alloy [51]. Furthermore, for 2D systems of group V elements, including blue phosphorus [52, 53], bismuthene, and antimonene on Au(111) [54], complex supercells, stripe-like arrangements, and substrate-induced stabilization of the 2D layer have been reported.

3 | Conclusion

We investigated the structural and chemical evolution of epitaxially grown submonolayer Sn on Au(111), with the Sn coverage precisely controlled by the post-deposition annealing temperature.

Our work focuses on the striped Sn phase, which, to the best of our knowledge, has not been reported previously. Combining STM, LEED, and XPS, we uncover a complex superstructure composed of different unit cells and building blocks with periodicities ranging from Rec($13 \times 2\sqrt{3}$) to Rec($19 \times 2\sqrt{3}$), with Rec($16 \times 2\sqrt{3}$) being the most common one. The phase consists of alternating honeycomb-like and square-like Sn regions, arranged in stripes with three rotational domains consistent with the Au(111) substrate symmetry. The honeycomb regions are atomically flat, and the determined Sn–Sn bond length matches well predictions from theory for freestanding stanene as well as with reports of flat stanene on Pd_2Sn(111) and Cu(111) [1, 13, 16].

XPS core-level analysis reveals that the striped phase shares nearly identical Au 4f and Sn 4d componental contributions

with the square-like X-phase, suggesting that both phases share common structural motifs. Based on this chemical similarity and the measured Sn coverage, we propose a model in which the square-like stripes grow atop a Au_2Sn surface alloy, while the honeycomb stripes form directly on the Au(111) surface. The striped phase, therefore, is an intermediate state between the square-like X-phase, which grows atop an Au_2Sn alloy layer, and the $\sqrt{7}$-phase, consisting of a single layer of Sn-dimers in a stretched honeycomb arrangement without alloying.

The observed alternating arrangement of square-like Sn and atomically flat honeycomb stanene might be interpreted as the first realization of zigzag stanene nanoribbons with widths of the honeycomb-stripe ranging from ≈ 1.5 nm to ≈ 3.2 nm. Moreover, our study provides the first experimental evidence of atomically flat, unstretched honeycomb stanene on Au(111).

Our results hint that alloying and dealloying at the Sn/Au(111) interface drives the structural arrangement of 2D Sn phases. Epitaxially grown Sn on Au(111) is found to be structurally versatile, and the Au_2Sn interface alloy stabilizes as supporting unusual surface reconstructions. Our insights provide pathways for preparing 2D stanene phases and potentially Sn nanoribbon architectures for future applications.

4 | Methods

The sample preparation and data acquisition were performed in situ using two different ultra-high vacuum (UHV) chambers. The setup used for XPS and valence band measurements had a base pressure of $p \leq 1 \times 10^{-10}$ mbar, while STM measurements were conducted in a separate chamber at $p \leq 5 \times 10^{-11}$ mbar. Both chambers were equipped with Low-Energy Electron Diffraction (LEED), argon ion sputtering, and resistive sample heating.

Identical sample preparation routines were followed across both systems, with minor adaptations to account for differences in chamber geometry. The LEED system in each chamber was used to determine the periodicity of the observed surface reconstructions. Because the structural phases are very sensitive to tin coverage, particularly below 1/3 ML Sn [24], calibration of deposition parameters was performed for each experimental setup.

4.1 | Sample Preparation

Clean Au(111) surfaces were prepared by repeated cycles of Ar^+ ion sputtering, followed by thermal annealing. Detailed preparation parameters are provided in the Supporting Information (Table S2). Tin was deposited by physical vapor deposition (PVD), with the deposition rate determined via a quartz crystal microbalance and maintained at approximately 3 $Å h^{-1}$. The Sn coverage was independently measured using XPS survey spectra, applying Fadley's approach for submonolayer coverage determination [55], as summarized by Zemlyanov et al. [56]. These measurements were performed at multiple emission angles (always at least $\Theta = 0°$ (normal emission) and $\Theta = 60°$ (grazing emission)), and the reported coverage value is the average of these measurements. The reported error corresponds to the standard deviation of these measurements. The detailed formulas and parameters used to determine the Sn coverage using XPS are given in the Supporting Information (Section S8).

4.2 | Sn Coverage Definition

The tin coverage is quantified in monolayers (ML), with one monolayer defined by the atomic density of the unreconstructed Au(111) surface, which is 1.391×10^{15} atoms/ cm^2. Using this standard, the deposition time required to form the square-like X-phase on top of the Au_2Sn interface alloy at a coverage of ≈ 0.66 ML is approximately 40 min in our experimental setup.

4.3 | XPS

X-ray photoelectron spectroscopy (XPS) data were measured at the endstation of beamline 11 at the DELTA synchrotron, TU Dortmund University, which provides linearly polarized soft X-rays ranging from 50 eV to 1500 eV from the U55 undulator which is tunable using a plane-grating monochromator [57]. The analysis chamber includes a five-axis manipulator, which has three translational and two rotational degrees of freedom, and is equipped with a hemispherical electron analyzer.

Survey spectra were recorded with a pass energy of 50 eV and a step size of $\Delta E = 1.22$ eV. High-resolution and valence band spectra were measured with a pass energy of 5 eV and $\Delta E = 41$ meV. Photon energies of $h\nu = 700$ eV, $h\nu = 240$ eV, and $h\nu = 52.5$ eV were used for survey, high-resolution core-level, and valence-band spectra, respectively. Measurements at normal emission ($\Theta = 0°$) probed bulk contributions, while grazing emission ($\Theta = 60°$) enhanced surface sensitivity.

High-resolution spectra were analyzed using the `LG4X-V2` Python package [58], which applies non-linear least-squares fitting based on the Levenberg–Marquardt algorithm using the `LMFIT` [59] and `lmfitxps` [60] python libraries. Each spectrum was modeled using Doniach–Šunjić line shapes [61], convoluted with a Gaussian function. For all spectra, a Tougaard background was used and included in the fit model to allow simultaneous optimization of peak and background parameters.

Identical values for full width at half maximum (FWHM) and asymmetry parameter β were applied to both components of each spin-orbit doublet. All obtained fit parameters are reported in the respective tables. All binding energies are referenced to the Fermi level. The position of the Fermi level was determined by fitting the Fermi edge, which was measured before and after each high-resolution data set. A detailed description is provided in the Supporting Information (Section S9).

The Gaussian contribution to the broadening of the Fermi edge, caused by the instrumental broadening, was used in core-level peak fitting, allowing only minor adjustments of less than 5%. Fit quality is indicated using the normalized residual $R(E)$ and the reduced chi-squared value $\chi^2_{\text{red.}}$ for each fitted spectrum.

4.4 | STM

Scanning tunneling microscopy (STM) was carried out at room temperature using a Scienta Omicron LT-STM [62, 63]. Tungsten tips were chemically etched in a 20% NaOH solution and sharpened further in situ by applying voltage pulses. STM images were recorded in constant current mode, with tunneling current and bias voltage set for each scan. Values for these parameters are provided in the corresponding figure captions. All images were recorded at a resolution of 400×400 pixels; the scan scale in [nm/Pixel] was adjusted for each measurement. The image processing, including plane correction, drift compensation, and Fourier transformation, was performed using the Gwyddion software package [64].

4.5 | Declaration of Generative AI and AI-Assisted Technologies in the Writing Process

During the preparation of this work, J.A.H. used Grammarly to assist with language improvements. All content was subsequently reviewed and edited by J.A.H., who takes full responsibility for the final version. No additional use of artificial intelligence was involved in the acquisition, analysis, or interpretation of data, or in any other aspect of this study.

Author Contributions

J.A.H.: Conceptualization, Data curation, Formal analysis, Investigation, Methodology, Project administration, Software, Visualization, Writing – original draft, S.H., A.K., and P.W.: Investigation, Writing–review and editing, U.B.: Writing–review and editing, H.H.: Resources, Supervision, Validation, Writing-review, and editing, C.W.: Funding acquisition, Resources, Supervision, Validation, Writing-review, and editing.

Acknowledgements

The authors thank the DELTA staff for supplying synchrotron radiation and for their support during beam times. J.A.H. also thanks Dr. Marie Schmitz and Dr. Lukas Kesper for their support during XPS measurements and their remarks regarding the XPS analysis.

Open access funding enabled and organized by Projekt DEAL.

Funding

Deutsche Forschungsgemeinschaft (DFG, German Research Foundation) – INST 212/458-1 FUGG; Land Nordrhein-Westfalen

Conflicts of Interest

The authors declare no conflicts of interest.

Data Availability Statement

The data that support the findings of this study are openly available at DOI:https://doi.org/10.5281/zenodo.17078270 10.5281/zenodo.17078270.

References

1. Y. Xu, "Large-Gap Quantum Spin Hall Insulators in Tin Films," *Physical Review Letters* 111, no. 13 (2013).

2. Y. Fang, Z.-Q. Huang, C.-H. Hsu, et al. "Quantum Spin Hall States in Stanene/Ge(111)," *Scientific Reports* 5, no. 1 (Sept 2015): 14196.

3. J. Wang, "Two-Dimensional Time-Reversal-Invariant Topological Superconductivity in a Doped Quantum Spin-Hall Insulator," *Physical Review B* 90, no. 5 (2014).

4. D. Zhou, H. Li, S. Bu, et al. "Phase Engineering of Epitaxial Stanene on a Surface Alloy," *The Journal of Physical Chemistry Letters* 12, no. 1 (Jan 2021): 211–217.

5. P. Borlido, A. W. Huran, M. A. L. Marques, and S. Botti, "Structural Prediction of Stabilized Atomically Thin Tin Layers," *npj 2D Materials and Applications* 3, no. 1 (May 2019): 1–5.

6. K. Quertite, H. Enriquez, N. Trcera, et al. "Silicene Nanoribbons on an Insulating Thin Film," *Advanced Functional Materials* 31, no. 7 (2021): 2007013.

7. D. J. Klaassen, L. Eek, A. N. Rudenko, et al. "Realization of a One Dimensional Topological Insulator in Ultrathin Germanene Nanoribbons," *Nature Communications* 16, no. 1 (Feb 2025): 2059.

8. M. Fadaie, N. Shahtahmassebi, M. Roknabad, and O. Gulseren, "First-Principles Investigation of Armchair Stanene Nanoribbons," *Physics Letters A* 382, no. 4 (Jan 2018): 180–185.

9. J. Qi, K. Hu, and X. Li, "Electric Control of the Edge Magnetization in Zigzag Stanene Nanoribbons from First Principles," *Physical Review Applied* 10, no. 3 (Sept 2018): 034048.

10. F. Rahimi and A. Phirouznia, "High Optical Spin-Filtering in Antiferro Magnetic Stanene Nanoribbons Induced by Band Bending and Uniaxial Strain," *Scientific Reports* 13, no. 1 (Aug 2023): 12874.

11. Y. Li, Z. Chen, X. Su, et al. "Edge-Passivation Modulation of the Transport Properties in Zigzag Stanene Nanoribbons," *Physical Review B* 109, no. 23 (June 2024): 235414.

12. F. Zhu, W. Chen, Y. Xu, et al. "Epitaxial Growth of Two-Dimensional Stanene," *Nature Materials* 14, no. 10 (Oct 2015): 1020–1025.

13. J. Deng, B. Xia, X. Ma, et al. "Epitaxial Growth of Ultraflat Stanene with Topological Band Inversion," *Nature Materials* 17, no. 12 (Dec 2018): 1081–1086.

14. J. Gou, "Strain–Induced Band Engineering in Monolayer Stanene on Sb(111)," *Physical Review Materials* 1, no. 5 (2017).

15. C.-Z. Xu, "Elemental Topological Dirac Semimetal: α-Sn on InSb(111)," *Physical Review Letters* 118, no. 14 (2017).

16. J. Yuhara, T. Ogikubo, M. Araidai, S. Takakura, M. Nakatake, and G. Le Lay, "In-Plane Strain-Free Stanene on a $Pd_2Sn(111)$ Surface Alloy," *Physical Review Materials* 5, no. 5 (May 2021): 053403.

17. S. Nigam, S. Gupta, D. Banyai, R. Pandey, and C. Majumder, "Evidence of a Graphene-Like Sn-Sheet on a Au(111) Substrate: Electronic Structure and Transport Properties From First Principles Calculations," *Physical Chemistry Chemical Physics* 17, no. 10 (Feb 2015): 6705–6712.

18. W. Pang, K. Nishino, T. Ogikubo, et al. "Epitaxial Growth of Honeycomb-Like Stanene on Au(111)," *Applied Surface Science* 517 (July 2020): 146224.

19. Y. Liu, N. Gao, J. Zhuang, et al. "Realization of Strained Stanene by Interface Engineering," *The Journal of Physical Chemistry Letters* 10, no. 7 (Apr 2019): 1558–1565.

20. P. Sadhukhan, D. Pandey, V. K. Singh, et al. "Electronic Structure and Morphology of Thin Surface Alloy Layers Formed by Deposition of Sn on Au(1 1 1)," *Applied Surface Science* 506 (Mar 2020): 144606.

21. J. Shah, W. Wang, H. M. Sohail, and R. I. G. Uhrberg, "Atomic and Electronic Structures of the Au2Sn Surface Alloy on Au(111)," *Physical Review B* 104, no. 12 (Sept 2021): 125408.

22. M. Maniraj, B. Stadtmüller, D. Jungkenn, et al. "A Case Study for the Formation of Stanene on a Metal Surface," *Communications Physics* 2, no. 1 (Feb 2019): 1–9.

23. J. A. Hochhaus, S. Hilgers, A. Kononov, et al. "First Evidence of a Square-Like Sn Lattice on the Au2Sn Surface Alloy on Au(111)," *Applied Surface Science* 714 (Dec 2025): 164470.

24. J. A. Hochhaus, S. Hilgers, M. Schmitz, L. Kesper, U. Berges, and C. Westphal, "Structural Analysis of Sn on Au(111) at Low Coverages: Towards the Au_2 Sn Surface Alloy with Alternating fcc and hcp Domains," *Scientific Reports* 15, no. 1 (Mar 2025): 7953.

25. M. Maniraj, D. Jungkenn, W. Shi, et al. "Structure and Electronic Properties of the $(\sqrt{3} \times \sqrt{3})$R30°$SnAu_2$ / Au(111) Surface Alloy," *Physical Review B* 98, no. 20 (Nov 2018): 205419.

26. J. Yuhara, Y. Fujii, K. Nishino, et al. "Large Area Planar Stanene Epitaxially Grown on Ag(1 1 1)," *2D Materials* 5, no. 2 (Jan 2018): 025002.

27. J. T. Küchle, A. Baklanov, A. P. Seitsonen, et al. "Silicene's Pervasive Surface Alloy on Ag(111): A Scaffold for Two-Dimensional Growth," *2D Materials* 9, no. 4 (Sept 2022): 45021.

28. L. Kesper, J. A. Hochhaus, M. Schmitz, M. G. H. Schulte, U. Berges, and C. Westphal, "Tracing the Structural Evolution of Quasi-Freestanding Germanene on Ag(111)," *Scientific Reports* 12, no. 1 (May 2022): 7559.

29. W. Egelhoff, "Core-Level Binding-Energy Shifts at Surfaces and in Solids," *Surface Science Reports* 6, no. 6–8, (May 1987): 253–415.

30. R. M. Friedman, J. Hudis, M. L. Perlman, and R. E. Watson, "Electronic Behavior in Alloys: Au-Sn," *Physical Review B* 8, no. 6 (Sept 1973): 2433–2440.

31. S. Chakraborty and K. S. Menon, "LEED and Photoemission Study of Growth and Structural Evolution of Sn on Ag(001)," *Vacuum* 125 (Mar 2016): 106–112.

32. S. Chakraborty and K. S. R. Menon, "Growth and Structural Evolution of Sn on Ag(001): Epitaxial Monolayer to Thick Alloy Film," *Journal of Vacuum Science & Technology, A: Vacuum, Surfaces, and Films* 34, no. 4 (July 2016): 41513.

33. F. Sette, G. K. Wertheim, Y. Ma, et al. "Lifetime and Screening of the C 1s Photoemission in Graphite," *Physical Review B* 41, no. 14 (May 1990): 9766–9770.

34. P. S. Bagus, E. S. Ilton, and C. J. Nelin, "The Interpretation of XPS Spectra: Insights into Materials Properties," *Surface Science Reports* 68, no. 2 (June 2013): 273–304.

35. S. Hüfner and G. K. Wertheim, "Core-Line Asymmetries in the X-Ray-Photoemission Spectra of Metals," *Physical Review B* 11, no. 2 (Jan 1975): 678–683.

36. J. A. Bearden and A. F. Burr, "Reevaluation of X-Ray Atomic Energy Levels," *Reviews of Modern Physics* 39, no. 1 (Jan 1967): 125–142.

37. C.-H. Lin, A. Huang, W. W. Pai, et al. "Single-Layer Dual Germanene Phases on Ag(111)," *Physical Review Materials* 2, no. 2 (Feb 2018): 024003.

38. J. Zhuang, C. Liu, Z. Zhou, et al. "Dirac Signature in Germanene on Semiconducting Substrate," *Advanced Science* 5, no. 7 (2018): 1800207.

39. T.-Y. Chen, D. Mikolas, S. Chiniwar, et al. "Germanene Structure Enhancement by Adjacent Insoluble Domains of Lead," *Physical Review Research* 3, no. 3 (Aug 2021): 033138.

40. K. Zhang, R. Bernard, Y. Borensztein, H. Cruguel, and G. Prévot, "Growth of Germanium-Silver Surface Alloys Followed by in Situ Scanning Tunneling Microscopy: Absence of Germanene Formation," *Physical Review B*, 102, no. 12 (Sept 2020): 125418.

41. P. Sadhukhan, S. Barman, T. Roy, et al. "Electronic Structure of Au-Sn Compounds Grown on Au(111)," *Physical Review B* 100, no. 23 (Dec 2019): 235404.

42. S. Hüfner, G. K. Wertheim, and J. H. Wernick, "XPS Core Line Asymmetries in Metals," *Solid State Communications* 17, no. 4 (Aug 1975): 417–422.

43. P. H. Citrin, G. K. Wertheim, and Y. Baer, "Core-Level Binding Energy and Density of States from the Surface Atoms of Gold," *Physical Review Letters* 41, no. 20 (Nov 1978): 1425–1428.

44. K. Hermann, "LEEDpat Download Package," (2022).

45. H. Walen, D.-J. Liu, J. Oh, et al. "Self-Organization of S Adatoms on Au(111): $\sqrt{3}$R30° Rows at Low Coverage," *The Journal of Chemical Physics* 143, no. 1 (July 2015): 014704.

46. P. M. Spurgeon, K. C. Lai, Y. Han, J. W. Evans, and P. A. Thiel, "Fundamentals of Au(111) Surface Dynamics: Coarsening of Two-Dimensional Au Islands," *The Journal of Physical Chemistry C* 124, no. 13 (Apr 2020): 7492–7499.

47. B. Feng, Z. Ding, S. Meng, et al. "Evidence of Silicene in Honeycomb Structures of Silicon on Ag(111)," *Nano Letters* 12, no. 7 (July 2012): 3507–3511.

48. R. Arafune, C.-L. Lin, K. Kawahara, et al. "Structural Transition of Silicene on Ag(111)," *Surface Science* 608 (Feb 2013): 297–300.

49. Z.-L. Liu, M.-X. Wang, C. Liu, et al. "The Fate of the $2\sqrt{3} \times 2\sqrt{3}$R(30°) Silicene Phase on Ag(111)," *APL Materials* 2, no. 9 (Sept 2014): 092513.

50. K. Zhang, M.-C. Hanf, R. Bernard, et al. "The Ground State of Epitaxial Germanene on Ag(111)," *ACS Nano* 17, no. 16 (Aug 2023): 15 687–15 695.

51. J. Yuhara, B. He, N. Matsunami, M. Nakatake, and G. Le Lay, "Graphene's Latest Cousin: Plumbene Epitaxial Growth on a "Nano WaterCube"," *Advanced Materials* 31, no. 27 (2019): 1901017.

52. J. L. Zhang, S. Zhao, S. Sun, et al. "Synthesis of Monolayer Blue Phosphorus Enabled by Silicon Intercalation," *ACS Nano* 14, no. 3 (Mar 2020): 3687–3695.

53. F. Yan, C. Zhao, P. Qin, et al. "Charge Transfer-Stabilized SiP Monolayer: An Unexpected Two-Dimensional Honeycomb on Au(111)," *Nano Letters* 25, no. 35 (Sept 2025): 13 347–13 354.

54. D. Zhou, N. Si, B. Jiang, X. Song, et al. "Interfacial Effects on the Growth of Atomically Thin Film: Group VA Elements on Au(111)," *Advanced Materials Interfaces* 6, no. 21 (Nov 2019): 1901050.

55. C. S. Fadley, "Basic Concepts of X-ray Photoelectron Spectroscopy," in *Electron Spectroscopy: Theory, Techniques and Applications* (New York: Academic Press, 1978), 1–156.

56. D. Y. Zemlyanov, M. Jespersen, D. N. Zakharov, et al. "Versatile Technique for Assessing Thickness of 2D Layered Materials by XPS," *Nanotechnology* 29, no. 11 (Mar 2018): 115705.

57. C. Westphal, U. Berges, S. Dreiner, et al. "The Plane-Grating Monochromator Beamline at the U55 Undulator for Surface and Interface Studies at DELTA," *Journal of Electron Spectroscopy and Related Phenomena* 144–147 (June 2005): 1117–1123.

58. J. A. Hochhaus and H. Nakajima, "LG4X-V2," Zenodo (Aug 2024).

59. M. Newville, R. Otten, A. Nelson, et al. "Lmfit/lmfit-py: 1.3.2," Zenodo (July 2024).

60. J. A. Hochhaus, "Lmfitxps," Zenodo, (Oct 2024).

61. S. Doniach and M. Sunjic, "Many-Electron Singularity in X-ray Photoemission and X-ray Line Spectra from Metals," *Journal of Physics C: Solid State Physics* 3, no. 2 (Feb 1970): 285.

62. T. Becker, H. Hövel, M. Tschudy, and B. Reihl, "Applications with a New Low-temperature UHV STM at 5 K," *Applied Physics A* 66, no. 1 (Mar 1998): S27–S30.

63. H. Hövel, T. Becker, D. Funnemann, B. Grimm, C. Quitmann, and B. Reihl, "High-Resolution Photoemission Combined with Low-Temperature STM," *Journal of Electron Spectroscopy and Related Phenomena* 88–91 (Mar 1998): 1015–1020.

64. D. Nečas and P. Klapetek, "Gwyddion: An Open-Source Software for SPM Data Analysis," *Open Physics* 10, no. 1 (Feb 2012): 181–188.

Supporting Information

Additional supporting information can be found online in the Supporting Information section.

Supporting Information